iScience

CellPress
OPEN ACCESS

Article

Bridging sheet size controls densification of MXene films for robust electromagnetic interference shielding

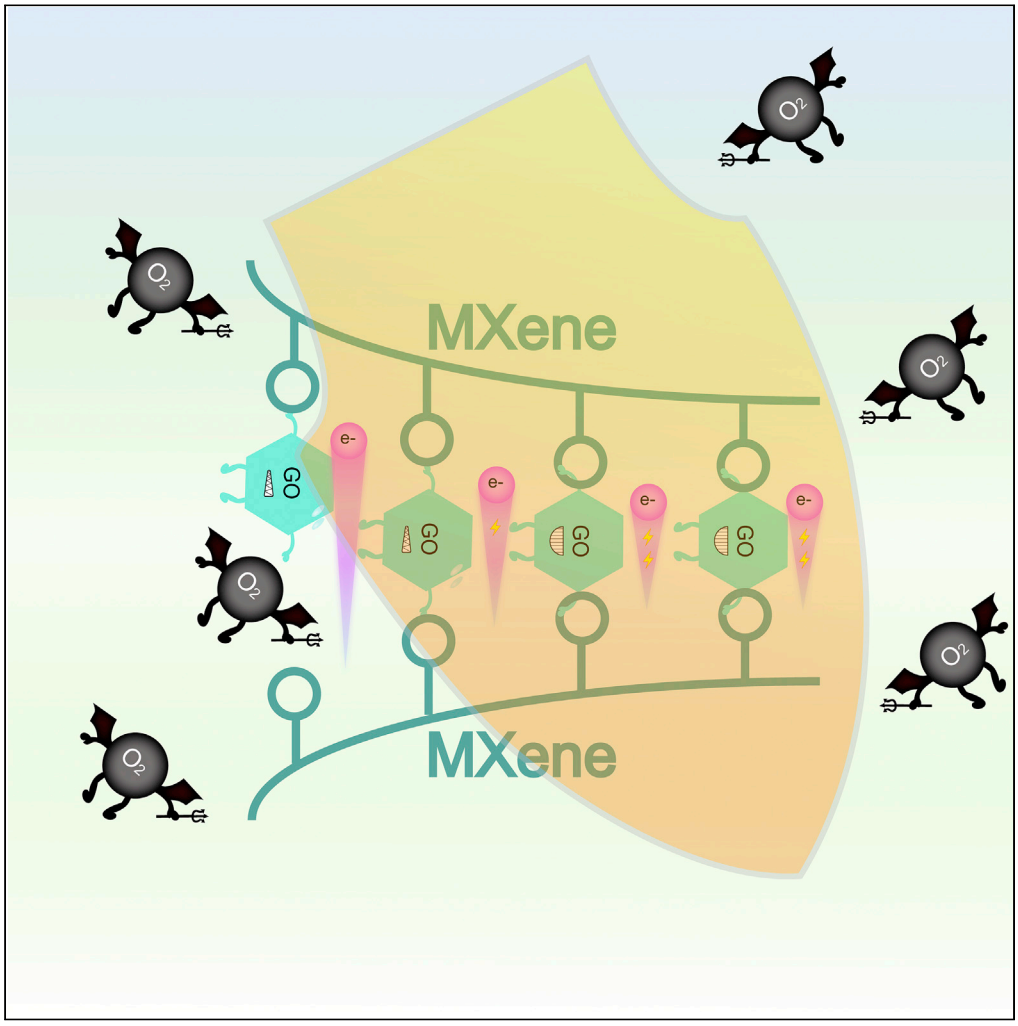

Bin Xia, Zhe Wang, Tingting Wang, ..., Bao-Wen Li, Zongkui Kou, Daping He

zongkuikou@whut.edu.cn (Z.K.)
hedaping@whut.edu.cn (D.H.)

Highlights

Densification of MXene films is controlled by a bridging-sheet-size strategy

Shortening electron-transport-distance in compact structure improves conductivity

Control of densification delivers high EMI shielding performance and air stability

Xia et al., iScience 25, 105001
September 16, 2022
https://doi.org/10.1016/j.isci.2022.105001

iScience

CellPress
OPEN ACCESS

Article

Bridging sheet size controls densification of MXene films for robust electromagnetic interference shielding

Bin Xia,[1,5] Zhe Wang,[1,5] Tingting Wang,[2,5] Shuaishuai Chen,[1] Han Wu,[3] Binbin Zhang,[3] Yunfa Si,[1] Zibo Chen,[1] Bao-Wen Li,[3] Zongkui Kou,[3,6,*] and Daping He[1,4,*]

SUMMARY

Numerous voids among the incompact layer-structure of MXene films result in their low ambient stability and poor innate conductivity for electromagnetic interference (EMI) shielding. Herein, we report a bridging-sheet-size-controlled densification process of MXene films by applying graphene oxide (GO) as a bridging agent. Specifically, the sheet size of GO is tailored to quantify a negative correlation of sheet size with densification for directing the preparation of most compact MXene-GO films. Benefiting from the shortest electron-transport-distance in the most compact structure, the conductivity of the MXene-GO film achieves 1.7 times (~1.6×10^5 S/m) that of MXene film. The EMI shielding performance (5.2×10^6 dB/m) reaches the record-value among reported MXene films at 10 μm-scale thickness. Moreover, the compact structure boosts the ambient stability of MXene-GO films where the conductivity and EMI shielding performance remain 88.7% and 90.0% after 15 days, respectively. The findings rationale the structure-activity relationship of compact MXene films for flexible electronics.

INTRODUCTION

With the rapid development of modern technology, various flexible electronic devices have been increasing dramatically (Sarycheva et al., 2018; Cao et al., 2018; Lee et al., 2020). The precise operation of these flexible electronic devices requires flexible electromagnetic interference (EMI) shielding materials with the properties of high conductivity, and ambient stability besides good mechanical flexibility (Wen et al., 2014; Shahzad et al., 2016; Xu et al., 2019). Nevertheless, conventional EMI shielding materials (such as metals) are increasingly difficult to meet the high mechanical flexibility requirement (Zhan et al., 2019; Jia et al., 2018; Lin et al., 2020; Wang et al., 2018).

MXene is a unique family of 2D transition metal carbides and/or nitrides (Liu et al., 2019a; Zhao et al., 2018, 2019; Yan et al., 2017; Weng et al., 2019), which has exhibited great potential in EMI shielding due to their high innate conductivity and excellent flexibility (Sambyal et al., 2019; Natu et al., 2019; Liu et al., 2018; He et al., 2019a, 2022). However, the numerous voids in the incompact MXene layer structure usually promote the oxidation reaction between surface termination (such as -OH, -*O*-, -F) of MXenes and oxygenated components in air (He et al., 2020; Xia et al., 2019; Persson et al., 2020; Lipatov et al., 2016; Seredych et al., 2019), producing a sharp decrease in the innate conductivity. A previous study has unveiled that when exposed to air at room temperature, the electrical conductivity (2.49×10^4 S m^{-1}) of the $Ti_3C_2T_x$ MXene film decays into ~7% after 27 days and <2% after 64th day (Habib et al., 2019). This seriously restricts the practical application of flexible MXene films. Structural densification induced by orderly bridging of bonding agents can reduce the area of the overall MXene film attacked by oxygen-containing components to a great extent, which is an effective strategy to improve the oxidation stability problem in air (Wan et al., 2021). Recently, Wan et al. reported that when placed in humid air for 10 days, the conductivity of the orderly bridged MXene films was maintained at ~ 86%, while that of the unbridged MXene films was only at ~ 20%. However, precisely controlling and understanding the densification of MXene films to synchronize the innate conductivity and ambient stability still remains an important challenge.

Herein, we find that the densification of MXene films induced by the bridging agent of graphene oxide (GO) is a sheet size-dependent process. Specifically, when the bridging GO sheet size decreased from 14.04 to

[1]Hubei Engineering Research Center of RF-Microwave Technology and Application, School of Science, Wuhan University of Technology, Wuhan 430070, China

[2]School of Mathematical & Physical Sciences, Wuhan Textile University, Wuhan 430200, China

[3]State Key Laboratory of Advanced Technology for Materials Synthesis and Processing, Wuhan University of Technology, Wuhan 430070, China

[4]State Key Laboratory of Silicate Materials for Architectures, Wuhan University of Technology, Wuhan 430070, China

[5]These authors contributed equally

[6]Lead contact

*Correspondence: zongkuikou@whut.edu.cn (Z.K.), hedaping@whut.edu.cn (D.H.)

https://doi.org/10.1016/j.isci.2022.105001

0.35 μm, the MXene-GO films become gradually more compact. We preferentially select the bridging agent of GO with nanoscale sheet size (0.35 μm) to achieve the elimination of the voids and the shortening of electron-transport-distance to the largest level, resulting in the enhanced conductivity. The conductivity of MXene-GO film can be improved to 1.7 times that of the pure MXene film. Moreover, the EMI shielding performance per unit thickness of MXene-GO film (5.2×10^6 dB/m) reaches the highest value in reported MXene films at 10 μm-scale thickness. More importantly, the compact structure greatly enhances the ambient stability of MXene-GO films, and the EMI shielding performance remained 88.7% and 90.0% after 15 days, respectively. We believe that this work shines a light on the development of dense and reliable MXene films with high conductivity and robust stability.

RESULTS

Bridging GO sheet-size controls densification of MXene films

$Ti_3C_2T_x$ MXene sheets were fabricated by selectively etching the Al layers from the Ti_3AlC_2 MAX phase using LiF/HCl solution. The successful etching and ultrasonic delamination were identified by scanning electronic microscopy (SEM) image and powder X-ray diffraction (XRD) pattern, as shown in Figures S1 and S2, respectively. Atomic force microscopic (AFM) and transmission electron microscopic (TEM) were then performed to confirm the monolayer $Ti_3C_2T_x$ sheets with a thickness of ~1.5 nm (Figures S3 and S4A). The high-crystalline nature and hexagonal structure were further revealed by selected-area electron diffraction pattern (Figure S4B). All these results demonstrate that the single-layer $Ti_3C_2T_x$ MXene sheets were successfully prepared.

We rationally screen graphene oxide (GO) nanosheets as bridging sheets to quantify the densification process of MXene. GO nanosheets dispersed in ultrapure water were added to MXene dispersion to obtain mixed MXene-GO dispersion. The mixed MXene-GO dispersion has an obvious Tyndall effect (Figure S5), which further verifies the stable interface interaction and uniform compound of MXene and GO. The mixed MXene-GO dispersion was prepared into flexible MXene-GO composite films via vacuum filtration method (Figure S6). Raman spectra in Figure S7 confirm the presence of GO nanosheets in the composite film.

We tuned the sheet size of bridging GO to quantify the structure-property relationship between sheet size and densification. We found that the sheet size of the bridging GO has a significant effect on the electrical conductivity of the MXene-GO film. When the sheet size of GO is nanoscale (0.35 μm, identified in the Figure S8), the conductivity of MXene-GO films reaches the highest value (Figure 1A). Particularly, as shown in Figure 1B, when the sheet size of bridging GO decreased from 14.04 to 0.35 μm, the interlayer distance gradually decreases, verifying that the MXene-GO films became more compact. In fact, during the forming process of MXene films, the MXene sheets are mainly affected by the capillary force and the electrostatic repulsion force as schematically shown in Figure 1C (Wu et al., 2021). Among them, the capillary force tends to make the stacking of MXene sheets denser, while the electrostatic repulsive force tends to make the stacking of MXene sheets looser. In terms of pure MXene films, the micron-scale MXene sheets are easily destabilized under the action of surface tension, which leads to non-densely stacking and porosity when assembled into macroscopic films. While GO sheets were introduced as bridging agent, the capillary force increases and electrostatic repulsion decreases, thus MXene-GO films possess more densely stacking structure due to the bridging of hydrogen bonds and the precisely tuned micro-zone force direction around the voids (Figure 1D). This mechanism is further confirmed by the water contact angle results and the zeta potential. As shown in Figures 1E and 1F, the water contact angle of MXene (57.9°) is 32.4% larger than that of MXene-GO (43.1°). Therefore, more hydrophilic MXene-GO films have stronger capillary forces. In addition, compared with the pure MXene film, MXene-GO film has a slightly lower Zeta potential (Figure 1G), indicating a weaker electrostatic repulsion force inside the MXene-GO film. Therefore, MXene-GO film with strongest capillary force and weakest electrostatic repulsion has a most compact structure for removing the numerous voids existed in the MXene film. The elimination of the voids and the shortening of electron-transport-distance can result in enhanced conductivity of MXene-GO film.

While the sheet size of the bridging GO increases to the micron-scale, the conductivity of the MXene-GO film decreased greatly, even lower than that of the pure MXene film. This is mainly related to the fact that insulating GO sheets with large sheet sizes hinder electron transport inside the MXene-GO film. In addition, the micron-scale GO sheets are also easily destabilized under the action of surface tension, which leads to less-densely stacking and porosity and lower conductivity (Figure 1D).

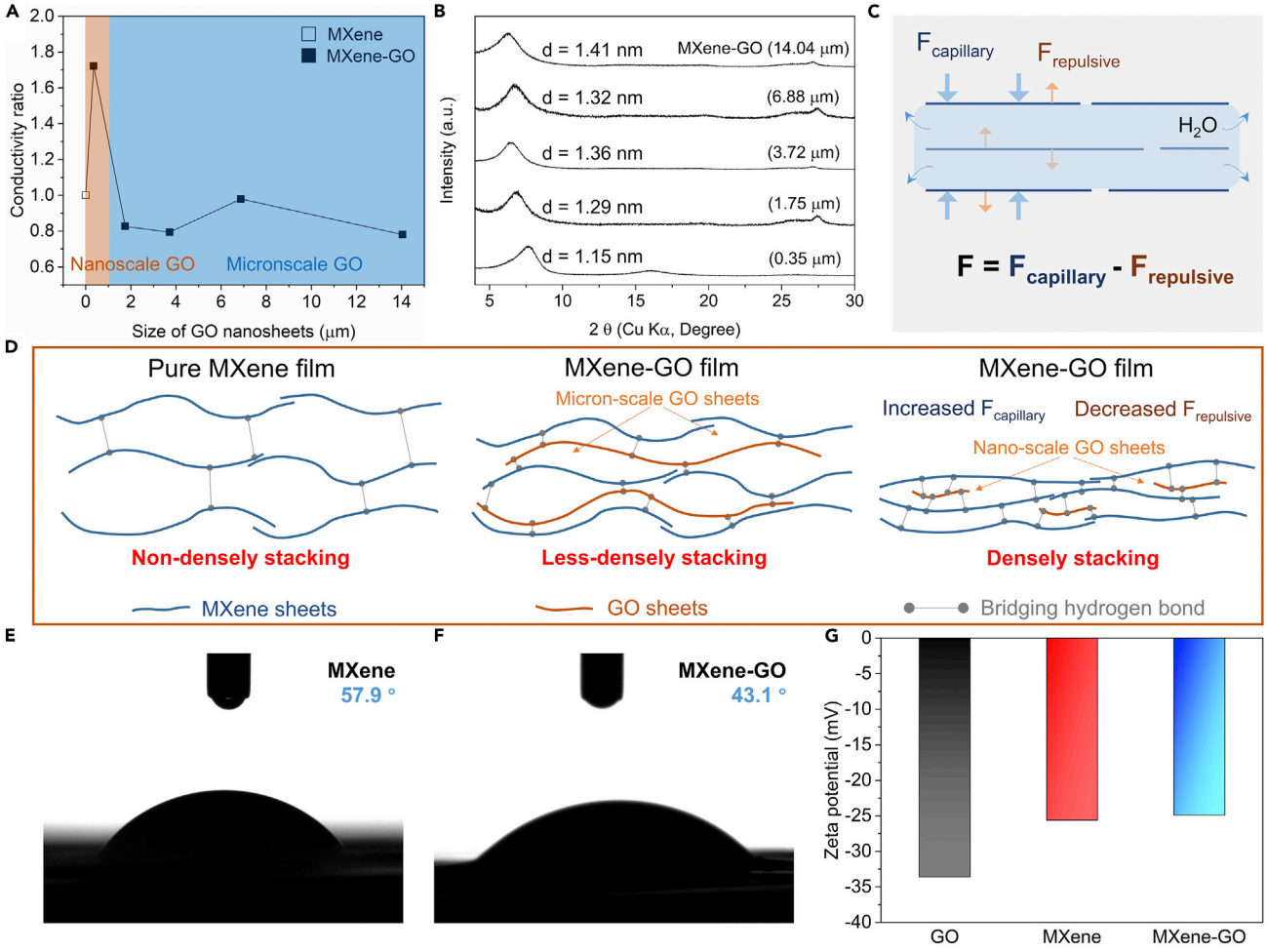

Figure 1. Densification process of MXene films after the introduction of GO sheets with different sheet sizes

(A) Electrical conductivities of MXene-GO films with different sizes of GO sheets.

(B) XRD patterns of MXene-GO films with different sizes of GO sheets.

(C) Schematic diagram of force analysis.

(D) Size effect of GO sheets on the densification in the forming process of pure MXene films and MXene-GO films.

(E, F) Water contact angle of MXene-GO film and pure MXene film.

(G) Zeta potential of MXene-GO dispersion and MXene dispersion.

We also explored the effect of GO content on the conductivity of MXene films. The MXene-GO film with 2, 4, 6, 8, and 10 wt % GO and the same sheet size was denoted as MXene-GO I, II, III, IV, and V, respectively. XRD pattern was conducted to provide structural information on the MXene-based films. As shown in Figure 2A, the (002) diffraction peak of MXene gradually shifts to a larger angle with an increase of GO content from 0 to 10 wt %. This corresponds to a decreased interlayer *d*-spacing of $Ti_3C_2T_x$ nanosheets, indicating successful insertion of GO sheets into the MXene layers, and formation of a uniform and compact layered structure. The GO nanosheet among neighboring MXene sheets promotes compact stacking by bridging MXene sheets together and thus composes a highly ordered MXene assembly, which is aligned along the in-plane direction. During GO filling, the internal voids could be prevented as much as possible. Consequently, the voids of MXene-GO composite films decrease gradually and the density of the MXene-GO composite films increases accordingly with the increase of GO content (Figure 2B). This is also confirmed by the scanning electron microscope (SEM) cross-section images of pure MXene film and MXene-GO film (Figures 2C–2F). The thickness of MXene film is 14 μm (Figure 2C), while the thickness of MXene-GO film is decreased to 10 μm after adding 8 wt % content of GO (Figure 2E). Significantly, the assembled layers of pure MXene film obtained by filtration were non-densely

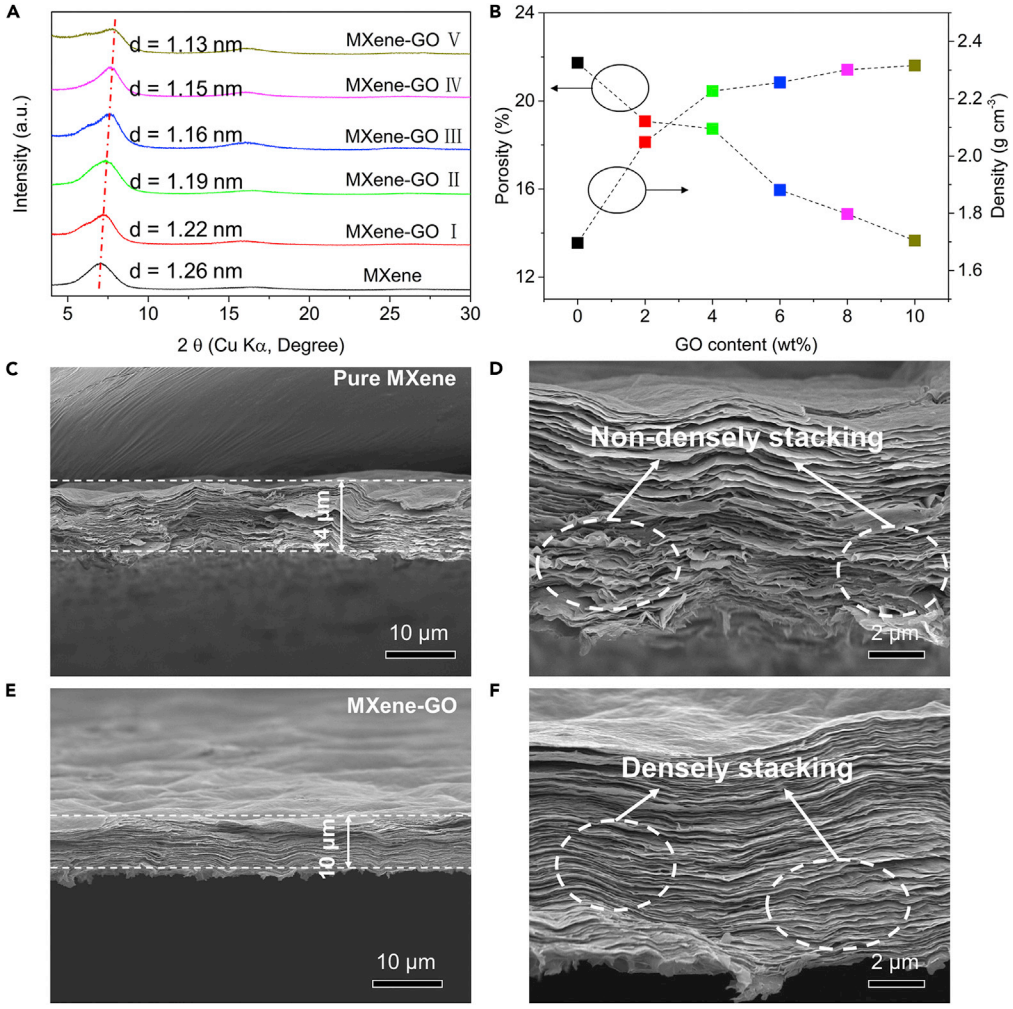

Figure 2. Densified MXene-GO films induced by nanoscale GO sheets

(A) XRD patterns of MXene-GO films with different GO content.

(B) Porosity of MXene-GO films with different GO content.

(C, D) Cross-sectional SEM images of pure MXene film.

(E, F) Cross-sectional SEM images of MXene-GO film.

stacking (Figure 2D). After bridging GO was implanted into interlayer of MXene film, as shown in Figure 2F, the parallel arrangement and densely stacking among layers of MXene-GO film suggested that the structure became more compact.

As shown in the surface structure model of MXene and MXene-GO film (Figure 3A), the MXene-GO films with denser structures also have flatter surfaces. Figures 3B and 3C show 3D super wide depth of field microscope images of pure MXene film and MXene-GO film, respectively. The surface of MXene film is not flat and presents a hilly morphology, while the surface of MXene-GO film is flat without frequent fluctuation in height and obvious wrinkles. The AFM images were used to further quantitatively determine the specific differences between the two surfaces (Figures 3D and 3E). The root means square surface roughness of MXene film is 80.2 nm, while that of MXene-GO film is only 24.7 nm. This suggests that the addition of bridging GO can not only make the interior of the MXene-GO film more compact but also make the surface of the MXene-GO film flatter. These results are consistent with the analyses of the SEM cross-sections, which indirectly confirm the dense structure of the MXene-GO films.

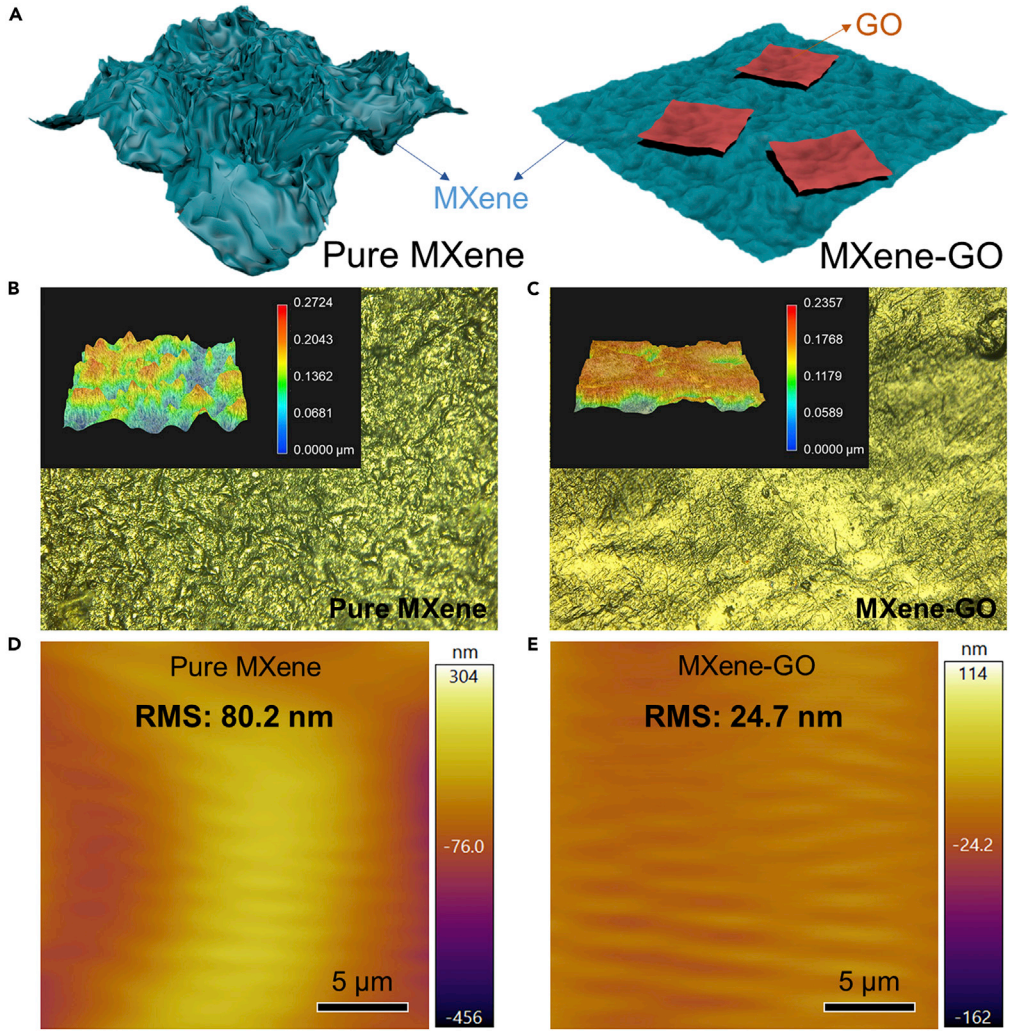

Figure 3. Surface structure of MXene-GO films

(A) Surface model diagram of MXene and MXene-GO film.

(B, C) 3D microscope images with super wide depth of field of MXene film and MXene-GO film.

(D, E) AFM images of MXene film and MXene-GO film.

Densification directs the synergistic enhancement of conductivity and ambient stability

More significantly, the high electrical conductivity of MXene is further improved by the implantation of bridging nanoscale GO. MXene-GO IV film exhibits 1.7 times (~1.6 × 10^5 S/m) higher conductivity than that of pure MXene film (Figures 4A and S9). This is surprising because GO has been demonstrated to be insulating. The nanoscale GO sheets that we screen, minimize the negative impact of the insulating properties of GO on the conductive path of MXene. In addition, due to hydrogen bonding and interaction force generated between MXene sheets and GO sheets, MXene-GO film is densified as a whole. The intercalation of GO into 2D MXene galleries narrows interlayer spacing and thereby enhances the electronic transport within MXene films, reducing the thickness and improving the conductivity.

For the purpose of investigating the EMI attenuation performances of the MXene-GO films, the scattering parameters (S_{11} and S_{21}) were used to calculate the absorption (A), reflection (R), and transmission (T) coefficients of the MXene-GO films. The dense MXene-GO films also hold great promise for EMI shielding, especially in X-band (8.2–12.4 GHz). The densified and conductive structure of MXene-GO enables enhanced shielding effectiveness even with the thinner thickness. Figure 4B shows the EMI SE of 10 μm thick MXene-GO IV film can reach 52.7 dB at 8.2 GHz, which is superior to 47.8 dB of pure MXene film

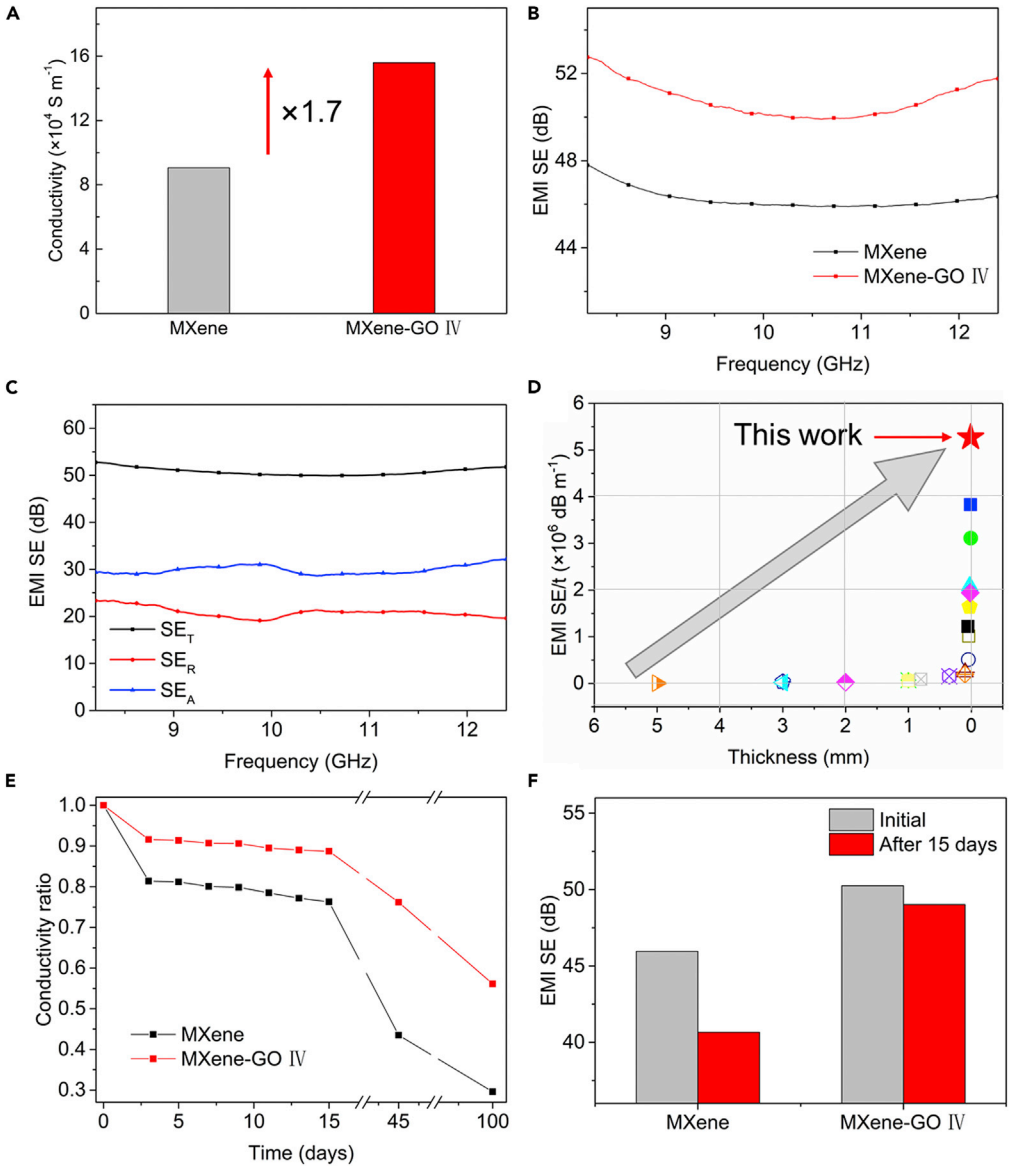

Figure 4. Conductivity and EMI SE of MXene-GO films

(A) Electrical conductivities of MXene film and MXene-GO IV film.

(B) EMI SE of MXene film and MXene-GO IV film.

(C) SE_T, SE_A, and SE_R of MXene-GO IV film.

(D) Comparison of EMI shielding effectiveness per unit thickness and the thickness of MXene-based films with those reported in the literature.

(E) Electrical conductivity changes after 100 days for MXene film and MXene-GO IV film.

(F) EMI SE changes over 15 days for MXene film and MXene-GO IV film.

with 14 μm thickness. Figure S10 exhibits the highest EMI SE value of MXene-GO films with 8 wt % GO contents, which agrees with Figure S9. The total EMI SE (SE_T) could be divided into absorption (SE_A), reflection (SE_R), and multiple reflections (SE_M). Absorption and reflection coefficients can be used to explore which parts is dominant in EMI, and the *R* values of MXene-GO films are higher than *A* that presents reflection dominant shielding mechanism rather than absorption. However, as shown in Figure 4C, the remarkably higher SE_A illustrates that all MXene-GO films mean a higher percentage of absorption of waves entering the films. The proportion of EMI absorption increases with the increase of GO contents (Figure S11). The remarkable EMI SE should be ascribed to the unique 2D layered structure and high conductivity of

MXene-GO film. The former makes the electromagnetic wave reflect multiple times internally between layers in the films, and the latter causes electrical loss and consumes the energy of the electromagnetic wave.

Modern flexible electronic equipment put forward higher requirements on the thickness (t) of EMI shielding films. EMI shielding films with high SE/t are competitive. Figure S12 shows that the SE/t of MXene-GO I to V films all reach >3.5 × 10^6 dB m^{-1}, and the value of most compact MXene-GO IV film reaches the highest (5.2 × 10^6 dB m^{-1}). As shown in Figure 4D and Table S1, the ultrathin and flexible MXene-GO composite film ranks at the top when compared with other MXene-based EMI shielding materials (Cao et al., 2019; Liu et al., 2019b; Fan et al., 2020; Han et al., 2019; Zhou et al., 2019; Jin et al., 2020; He et al., 2020; Xie et al., 2019).

In addition to the remarkable EMI shielding performances, we also explored the ambient stability of MXene-GO films. This is another significant issue for the practical application but relatively undervalued yet. Oxidation of MXene is known to be the main reason for the poor ambient stability, which damages the excellent conductivity. Our compact MXene-GO films exhibit excellent oxidation resistance. We exposed both pure MXene film and compact MXene-GO film to the air at the same time. The conductivity of MXene film has gradually decreased to 76.3% of the initial conductivity after 15 days, while that of MXene-GO film remains at 88.7% (Figure 4E). When the placement time reaches 100 days (Figure S13), the conductivity of MXene-GO film remained 46.2%, while that of MXene film was only 29.6%. As shown in Figure 4F, the decrease rate of EMI SE was also effectively retarded within 15 days. The EMI SE of MXene film is reduced by ~50%, while that of MXene-GO film is only reduced by ~10%. This shows that the addition of GO can effectively alleviate the oxidation rate of MXene in the air and improve the anti-oxidative stability.

DISCUSSION

We controlled the bridging-induced densification process of MXene films for removing the voids by applying graphene oxide (GO) nanosheets with different sheet sizes, therefore preparing a most compact MXene-GO film with remarkable EMI shielding effectiveness and robust EMI shielding capability. MXene-GO film has an electrical conductivity of 1.7 times (~1.6 × 10^5 S/m) higher than that of the incompact MXene film. In addition, MXene-GO film possesses an excellent EMI shielding performance per unit thickness (5.2 × 10^6 dB/m), which reaches the highest value in reported MXene films at 10 μm-scale thickness. Moreover, the slower rate of descent in conductivity and EMI SE of MXene-GO film is detected after 15 and 100 days in the air, indicating more robust ambient stability of MXene-GO film in practical application. Thus, the highly stable MXene-GO film with excellent EMI shielding performance will greatly widen the practical applications in the fields of aerospace, smart electronics, and wearable devices.

Limitations of the study

In our work, the size and shape of MXene film are limited by the preparation method, so the actual efficiency of this method needs to be improved in mass production of larger size films.

STAR★METHODS

Detailed methods are provided in the online version of this paper and include the following:

- KEY RESOURCES TABLE
- RESOURCE AVAILABILITY
  - Lead contact
  - Materials availability
  - Data and code availability
- METHOD DETAILS
  - Materials
  - Fabrication of MXene-GO film
  - Characterization
- QUANTIFICATION AND STATISTICAL ANALYSIS

SUPPLEMENTAL INFORMATION

Supplemental information can be found online at https://doi.org/10.1016/j.isci.2022.105001.

ACKNOWLEDGMENTS

The authors acknowledge financial support from the National Natural Science Foundation of China (51672204, 52172124), the Fundamental Research Funds for the Central Universities (WUT: 2020IB005, 2021III019JC), and the Foundation of National Key Laboratory on Electromagnetic Environment Effects (NO. 614220504030617). The authors also acknowledge the Center for Materials Research and Analysis at the Wuhan University of Technology for TEM and image suggestions from Dr. Xiaoqing Liu.

AUTHOR CONTRIBUTIONS

B.X., Z.W., and T.T.W. contributed equally to this work. B.X. and D.P.H. designed the project. B.X., S.S.C., H.W., B.B.Z., and Y.F.S. performed the preparation of materials and data analysis. B.X., Z.W., Z.B.C., H.W., and B.B.Z. carried out the characterization and measurement. Z.W., T.T.W., Z.K.K., and D.P.H. reviewed the manuscript. Z.K.K. and D.P.H. supervised the whole process.

DECLARATION OF INTERESTS

The authors declare no conflict of interest.

Received: June 15, 2021
Revised: August 1, 2022
Accepted: August 18, 2022
Published: September 16, 2022

REFERENCES

Akbari, A., Cunning, B.V., Joshi, S.R., Wang, C., Camacho-Mojica, D.C., Chatterjee, S., Modepalli, V., Cahoon, C., Bielawski, C.W., Bakharev, P., et al. (2020). Highly ordered and dense thermally conductive graphitic films from a graphene oxide/reduced graphene oxide mixture. Matter *2*, 1198–1206. https://doi.org/10.1016/j.matt.2020.02.014.

Cao, W., Ma, C., Tan, S., Ma, M., Wan, P., and Chen, F. (2019). Ultrathin and flexible CNTs/MXene/cellulose nanofibrils composite paper for electromagnetic interference shielding. Nano-Micro Lett. *11*, 72. https://doi.org/10.1007/s40820-019-0304-y.

Cao, W.T., Chen, F.F., Zhu, Y.J., Zhang, Y.G., Jiang, Y.Y., Ma, M.G., and Chen, F. (2018). Binary strengthening and toughening of MXene/cellulose nanofiber composite paper with nacre-inspired structure and superior electromagnetic interference shielding properties. ACS Nano *12*, 4583–4593. https://doi.org/10.1021/acsnano.8b00997.

Ding, L., Wei, Y., Wang, Y., Chen, H., Caro, J., and Wang, H. (2017). A two-dimensional lamellar membrane: MXene nanosheet stacks. Angew. Chem. Int. Ed. Engl. *56*, 1825–1829. https://doi.org/10.1002/anie.201609306.

Fan, Z., Wang, D., Yuan, Y., Wang, Y., Cheng, Z., Liu, Y., and Xie, Z. (2020). A lightweight and conductive MXene/graphene hybrid foam for superior electromagnetic interference shielding. Chem. Eng. J. *381*, 122696. https://doi.org/10.1016/j.cej.2019.122696.

Habib, T., Zhao, X., Shah, S.A., Chen, Y., Sun, W., An, H., Lutkenhaus, J.L., Radovic, M., and Green, M.J. (2019). Oxidation stability of Ti_3C_2Tx MXene nanosheets in solvents and composite films. npj 2D Mater. Appl. *3*, 8. https://doi.org/10.1038/s41699-019-0089-3.

Han, M., Yin, X., Hantanasirisakul, K., Li, X., Iqbal, A., Hatter, C.B., Anasori, B., Koo, C.M., Torita, T., Soda, Y., et al. (2019). Anisotropic MXene aerogels with a mechanically tunable ratio of electromagnetic wave reflection to absorption. Adv. Opt. Mater. *7*, 1900267. https://doi.org/10.1002/adom.201900267.

He, P., Cao, M.S., Cai, Y.Z., Shu, J.C., Cao, W.Q., and Yuan, J. (2020). Self-assembling flexible 2D carbide MXene film with tunable integrated electron migration and group relaxation toward energy storage and green EMI shielding. Carbon *157*, 80–89. https://doi.org/10.1016/j.carbon.2019.10.009.

He, P., Cao, M.S., Shu, J.C., Cai, Y.Z., Wang, X.X., Zhao, Q.L., and Yuan, J. (2019a). Atomic layer tailoring titanium carbide MXene to tune transport and polarization for utilization of electromagnetic energy beyond solar and chemical energy. ACS Appl. Mater. Interfaces *11*, 12535–12543. https://doi.org/10.1021/acsami.9b00593.

He, P., Liu, Z.Y., Mao, G.B., Liu, Q., Zheng, M.J., Zuo, R.Z., Cao, W.Q., Hou, Z.L., Yuan, J., and Cao, M.S. (2022). MXene films: toward high-performance electromagnetic interference shielding and supercapacitor electrode. Compos. Appl. Sci. Manuf. *157*, 106935. https://doi.org/10.1016/j.compositesa.2022.106935.

He, P., Wang, X.X., Cai, Y.Z., Shu, J.C., Zhao, Q.L., Yuan, J., and Cao, M.S. (2019b). Tailoring $Ti_3C_2T_x$ nanosheets to tune local conductive network as an environmentally friendly material for highly efficient electromagnetic interference shielding. Nanoscale *11*, 6080–6088. https://doi.org/10.1039/c8nr10489a.

Jia, L.C., Yan, D.X., Liu, X., Ma, R., Wu, H.Y., and Li, Z.M. (2018). Highly efficient and reliable transparent electromagnetic interference shielding film. ACS Appl. Mater. Interfaces *10*, 11941–11949. https://doi.org/10.1021/acsami.8b00492.

Jin, X., Wang, J., Dai, L., Liu, X., Li, L., Yang, Y., Cao, Y., Wang, W., Wu, H., and Guo, S. (2020). Flame-retardant poly (vinyl alcohol)/MXene multilayered films with outstanding electromagnetic interference shielding and thermal conductive performances. Chem. Eng. J. *380*, 122475. https://doi.org/10.1016/j.cej.2019.122475.

Lee, G.S., Yun, T., Kim, H., Kim, I.H., Choi, J., Lee, S.H., Lee, H.J., Hwang, H.S., Kim, J.G., Kim, D.W., et al. (2020). Mussel inspired highly aligned $Ti_3C_2T_x$ MXene film with synergistic enhancement of mechanical strength and ambient stability. ACS Nano *14*, 11722–11732. https://doi.org/10.1021/acsnano.0c04411.

Li, X., Yin, X., Liang, S., Li, M., Cheng, L., and Zhang, L. (2019). 2D carbide MXene Ti_2CT_x as a novel high-performance electromagnetic interference shielding material. Carbon *146*, 210–217. https://doi.org/10.1016/j.carbon.2019.02.003.

Lin, Z., Liu, J., Peng, W., Zhu, Y., Zhao, Y., Jiang, K., Peng, M., and Tan, Y. (2020). Highly stable 3D $Ti_3C_2T_x$ MXene-based foam architectures toward high-performance terahertz radiation shielding. ACS Nano *14*, 2109–2117. https://doi.org/10.1021/acsnano.9b08832.

Lipatov, A., Alhabeb, M., Lukatskaya, M.R., Boson, A., Gogotsi, Y., and Sinitskii, A. (2016). Effect of synthesis on quality, electronic properties and environmental stability of individual monolayer Ti_3C_2 MXene flakes. Adv. Electron. Mater. *2*, 1600255. https://doi.org/10.1002/aelm.201600255.

Liu, J., Liu, Z., Zhang, H., Chen, W., Zhao, Z., Wang, Q., and Yu, Z. (2019a). Ultrastrong and highly conductive MXene-based films for high-performance electromagnetic interference shielding. Adv. Electron. Mater. *6*, 1901094. https://doi.org/10.1002/aelm.201901094.

Liu, J., Zhang, H.B., Sun, R., Liu, Y., Liu, Z., Zhou, A., and Yu, Z.Z. (2017). Hydrophobic, flexible, and lightweight MXene foams for high-performance electromagnetic-interference shielding. Adv. Mater. *29*, 1702367. https://doi.org/10.1002/adma.201702367.

Liu, L., Chen, W., Zhang, H., Wang, Q., Guan, F., and Yu, Z. (2019b). Flexible and multifunctional silk textiles with biomimetic leaf-like MXene/silver nanowire nanostructures for electromagnetic interference shielding, humidity monitoring, and self-derived hydrophobicity. Adv. Funct. Mater. *29*, 1905197. https://doi.org/10.1002/adfm.201905197.

Liu, R., Miao, M., Li, Y., Zhang, J., Cao, S., and Feng, X. (2018). Ultrathin biomimetic polymeric $Ti_3C_2T_x$ MXene composite films for electromagnetic interference shielding. ACS Appl. Mater. Interfaces *10*, 44787–44795. https://doi.org/10.1021/acsami.8b18347.

Natu, V., Hart, J.L., Sokol, M., Chiang, H., Taheri, M.L., and Barsoum, M.W. (2019). Edge capping of 2D-MXene sheets with polyanionic salts to mitigate oxidation in aqueous colloidal suspensions. Angew. Chem. Int. Ed. Engl. *58*, 12655–12660. https://doi.org/10.1002/anie.201906138.

Persson, I., Halim, J., Hansen, T.W., Wagner, J.B., Darakchieva, V., Palisaitis, J., Rosen, J., and Persson, P.O. (2020). How much oxygen can a MXene surface take before it breaks? Adv. Funct. Mater. *30*, 1909005. https://doi.org/10.1002/adfm.201909005.

Sambyal, P., Iqbal, A., Hong, J., Kim, H., Kim, M.K., Hong, S.M., Han, M., Gogotsi, Y., and Koo, C.M. (2019). Ultralight and mechanically robust $Ti_3C_2T_x$ hybrid aerogel reinforced by carbon nanotubes for electromagnetic interference shielding. ACS Appl. Mater. Interfaces *11*, 38046–38054. https://doi.org/10.1021/acsami.9b12550.

Sarycheva, A., Polemi, A., Liu, Y., Dandekar, K., Anasori, B., and Gogotsi, Y. (2018). 2D titanium carbide (MXene) for wireless communication. Sci. Adv. *4*, eaau0920. https://doi.org/10.1126/sciadv.aau0920.

Seredych, M., Shuck, C.E., Pinto, D., Alhabeb, M., Precetti, E., Deysher, G., Anasori, B., Kurra, N., and Gogotsi, Y. (2019). High-temperature behavior and surface chemistry of carbide MXenes studied by thermal analysis. Chem. Mater. *31*, 3324–3332. https://doi.org/10.1021/acs.chemmater.9b00397.

Shahzad, F., Alhabeb, M., Hatter, C.B., Anasori, B., Man Hong, S., Koo, C.M., and Gogotsi, Y. (2016). Electromagnetic interference shielding with 2D transition metal carbides (MXenes). Science *353*, 1137–1140. https://doi.org/10.1126/science.aag2421.

Wan, S., Li, X., Chen, Y., Liu, N., Du, Y., Dou, S., Jiang, L., and Cheng, Q. (2021). High-strength scalable MXene films through bridging-induced densification. Science *374*, 96–99. https://doi.org/10.1126/science.abg2026.

Wang, Z., Mao, B., Wang, Q., Yu, J., Dai, J., Song, R., Pu, Z., He, D., Wu, Z., and Mu, S. (2018). Ultrahigh conductive copper/large flake size graphene heterostructure thin-film with remarkable electromagnetic interference shielding effectiveness. Small *14*, 1704332. https://doi.org/10.1002/smll.201704332.

Wen, B., Cao, M., Lu, M., Cao, W., Shi, H., Liu, J., Wang, X., Jin, H., Fang, X., Wang, W., and Yuan, J. (2014). Reduced graphene oxides: light-weight and high efficiency electromagnetic interference shielding at elevated temperatures. Adv. Mater. *26*, 3484–3489. https://doi.org/10.1002/adma.201400108.

Weng, C., Wang, G., Dai, Z., Pei, Y., Liu, L., and Zhang, Z. (2019). Buckled AgNW/MXene hybrid hierarchical sponges for high-performance electromagnetic interference shielding. Nanoscale *11*, 22804–22812. https://doi.org/10.1039/c9nr07988b.

Wu, Z., Liu, X., Shang, T., Deng, Y., Wang, N., Dong, X., Zhao, J., Chen, D., Tao, Y., and Yang, Q. (2021). Reassembly of MXene hydrogels into flexible films towards compact and ultrafast supercapacitors. Adv. Funct. Mater. *31*, 2102874. https://doi.org/10.1002/adfm.202102874.

Xia, F., Lao, J., Yu, R., Sang, X., Luo, J., Li, Y., and Wu, J. (2019). Ambient oxidation of Ti_3C_2 MXene initialized by atomic defects. Nanoscale *11*, 23330–23337. https://doi.org/10.1039/c9nr07236e.

Xie, F., Jia, F., Zhuo, L., Lu, Z., Si, L., Huang, J., Zhang, M., and Ma, Q. (2019). Ultrathin MXene/aramid nanofiber composite paper with excellent mechanical properties for efficient electromagnetic interference shielding. Nanoscale *11*, 23382–23391. https://doi.org/10.1039/c9nr07331k.

Xu, H., Yin, X., Li, X., Li, M., Liang, S., Zhang, L., and Cheng, L. (2019). Lightweight Ti_2CT_x MXene/poly (vinyl alcohol) composite foams for electromagnetic wave shielding with absorption-dominated feature. ACS Appl. Mater. Interfaces *11*, 10198–10207. https://doi.org/10.1021/acsami.8b21671.

Yan, J., Ren, C.E., Maleski, K., Hatter, C.B., Anasori, B., Urbankowski, P., Sarycheva, A., and Gogotsi, Y. (2017). Flexible MXene/graphene films for ultrafast supercapacitors with outstanding volumetric capacitance. Adv. Funct. Mater. *27*, 1701264. https://doi.org/10.1002/adfm.201701264.

Zhan, Z., Song, Q., Zhou, Z., and Lu, C. (2019). Ultrastrong and conductive MXene/cellulose nanofiber films enhanced by hierarchical nanoarchitecture and interfacial interaction for flexible electromagnetic interference shielding. J. Mater. Chem. C *7*, 9820–9829. https://doi.org/10.1039/c9tc03309b.

Zhao, S., Zhang, H.B., Luo, J.Q., Wang, Q.W., Xu, B., Hong, S., and Yu, Z.Z. (2018). Highly electrically conductive three-dimensional $Ti_3C_2T_X$ MXene/reduced graphene oxide hybrid aerogels with excellent electromagnetic interference shielding performances. ACS Nano *12*, 11193–11202. https://doi.org/10.1021/acsnano.8b05739.

Zhao, X., Vashisth, A., Prehn, E., Sun, W., Shah, S.A., Habib, T., Chen, Y., Tan, Z., Lutkenhaus, J.L., Radovic, M., and Green, M.J. (2019). Antioxidants unlock shelf-stable $Ti_3C_2T_x$ (MXene) nanosheet dispersions. Matter *1*, 513–526. https://doi.org/10.1016/j.matt.2019.05.020.

Zhou, B., Zhang, Z., Li, Y., Han, G., Feng, Y., Wang, B., Zhang, D., Ma, J., and Liu, C. (2020). Flexible, robust, and multifunctional electromagnetic interference shielding film with alternating cellulose nanofiber and MXene layers. ACS Appl. Mater. Interfaces *12*, 4895–4905. https://doi.org/10.1021/acsami.9b19768.

Zhou, Z., Liu, J., Zhang, X., Tian, D., Zhan, Z., and Lu, C. (2019). Ultrathin MXene/calcium alginate aerogel film for high-performance electromagnetic interference shielding. Adv. Mater. Interfaces *6*, 1802040. https://doi.org/10.1002/admi.201802040.

STAR★METHODS

KEY RESOURCES TABLE

REAGENT or RESOURCE	SOURCE	IDENTIFIER
Chemicals, peptides, and recombinant proteins		
Ti_3AlC_2	11 Technology	CAS: 196,506-01-1
graphene oxide	Wuxi Chengyi education technology	CAS: 7782-42-5
hydrochloric acid solution	Sinopharm	CAS: 7647-01-0
lithium fluoride	Aladdin	CAS: 7789-24-4
Software and algorithms		
Origin	OriginLab Corporation	https://www.originlab.com/

RESOURCE AVAILABILITY

Lead contact

Further information and requests for resources and reagents should be directed to and will be fulfilled by the lead contact, Zongkui Kou (zongkuikou@whut.edu.cn).

Materials availability

This study did not generate new unique reagents.

Data and code availability

- Data reported in this paper will be shared by the lead contact upon request.
- This paper does not report original code.
- Any additional information required to reanalyze the data reported in this paper is available from the lead contact upon request.

METHOD DETAILS

Materials

The multilayered $Ti_3C_2T_x$ MXene was obtained by selectively etching Ti_3AlC_2 MAX phase (Liu et al., 2017; Ding et al., 2017; Li et al., 2019; Zhou et al., 2020) according to the following method. First, 10 mL deionized (DI) water was added to 30 mL hydrochloric acid solution (HCl; 37 wt %) with the concentration of 12 M to obtain 9 M HCl solution. Then 2 g lithium fluoride (LiF; $\geq$ 99%) powder was dissolved in the HCl solution and stirred for half an hour at room temperature as an etching agent. After that, 2 g Ti_3AlC_2 MAX powder purchased from 11 Technology Co., Ltd. in China was slowly added into the etching agent, and the mixture was allowed to proceed at 40°C for 36 h under stirring. The resultant slurry was washed repeatedly using DI water and centrifuged at 3500 rpm for 5 min until the pH of upper supernatant reaches about 6. $Ti_3C_2T_x$ nanosheets were obtained by ultrasonication of re-dispersed black swelled clay-like sediment in ice bath for 15 min. The uniform delaminated $Ti_3C_2T_x$ MXene colloidal dispersion was obtained by centrifuging at 3500 rpm for 30 min.

Fabrication of MXene-GO film

The concentrations of GO and MXene in their aqueous suspensions are 1 mg mL^{-1} and 10 mg mL^{-1}, respectively. After GO suspension was added into MXene suspension drop by drop, the resultant MXene-GO suspension was stirred for 1 h. Subsequently, vacuum-assisted filtration was applied to assemble the homogeneous suspension of MXene sheets and GO sheets into freestanding hybrid films. After drying in vacuum oven at 50°C, the freestanding and flexible MXene-GO hybrid films were easily peeled off from the filter paper. The flexible composite films with different GO content were obtained through vacuum-assisted filtration. The composite films with 2, 4, 6, 8, and 10 wt % were designated as MXene-GO I, II, III, IV, and V respectively.

Characterization

Morphology and structure of films were observed with a field-emission scanning electron microscope (FESEM, JEOL JSM-7610FPlus) and a transmission electron microscope (TEM, JEOL JEM-1400Plus). The phase compositions of the samples were analyzed by an X-ray diffractometer (XRD, Rigaku Smartlab SE) with a Cu Kα radiation (λ = 1.54178 Å). The porosity of samples was determined by using density and XRD interlayer spacing. The XRD density of each sample, ρ_x, was calculated from the position of the (002) reflection of the film (Akbari et al., 2020).

$$\rho_x = \left(9.8\ \text{Å} \,/\, \text{sampale}\ d_{002}\right) \times 3.968\ g\ cm^{-3}$$
$$V = \left(1 \,/\, \rho_g - 1 \,/\, \rho_x\right)$$
$$P = V \times \rho_g \times 100\%$$

where, 9.8 Å and 3.968 g cm^{-3} are the d_{002} spacing and atomic density of crystalline hexagonal MXene, ρ_g is the sample density, and V and P are total pore volume and total % porosity of the sample.

Raman spectra were obtained with a RENISHAW InVia Raman microscope. In Figure S7, MXene film and MXene-GO film exhibit similar Raman spectra at 800 cm^{-1}. Specifically, the modes at 203 (ω_2) and 721 cm^{-1} (ω_3) are A_{1g} symmetry out-of-plane vibrations of Ti and C atoms, respectively, while the modes at 282 (ω_5), 372 (ω_5), and 624 cm^{-1}(ω_4) are all the E_g group vibrations, including in-plane (shear) modes of Ti, C, and surface functional group atoms. After the incorporation of GO nanosheets, two broad bands appear at ~1312 cm^{-1} and 1598 cm^{-1} for the MXene-GO, which are the characteristics for the D and G bands of GO, respectively. This confirms the presence of GO nanosheets in the composite film. The samples were also characterized by an atomic force microscopic (AFM, Oxford Cypher ES). The sheet resistance (R_s) was measured by using a four-point probe (RTS-8, Guangzhou Four Point Probe Technology Co., Ltd., China). The EMI SE results of films were tested by the N5224B vector network analyzer using the transmittance-reflection-load technique at both ends of the waveguide. The measured frequency ranges were X-band (8.2–12.4 GHz), and EMI SE of the material is often used to investigate the efficiency of the shield materials, which is a judgment of the ability to dissipate EM wave. Based on the measured *S* parameters, the EMI SE can be obtained by (He et al., 2019b):

$$R = \left|S_{11}\right|^2 = \left|S_{22}\right|^2$$
$$T = \left|S_{12}\right|^2 = \left|S_{21}\right|^2$$
$$R + A + T = 1$$
$$EMI\ SE = 10log\left(\frac{P_I}{P_T}\right) = 10log\left(\frac{1}{T}\right)$$

Where *R*, *A*, and *T* represent the reflection, absorption, and transmission coefficients, respectively. P_I is the incident power and P_T is the transmitted power.

The total SE (SE_T) and its components of absorption (SE_A) and reflection (SE_R) were determined based on the measured *S* parameters. For revealing the *SE* of SE_R and SE_A in detail, the *SE* in dB can also be achieved by

$$A_{eff} = \frac{1 - R - T}{1 - R}$$
$$SE_T = SE_A + SE_R + SE_M$$
$$SE_R = -10log(1 - R) = -10log\left(1 - \left|S_{11}\right|^2\right)$$
$$SE_A = -10log(1 - A_{eff}) = -10log\left(\frac{T}{1 - R}\right) = -10log\left(\frac{\left|S_{12}\right|^2}{1 - \left|S_{11}\right|^2}\right)$$

where A_{eff} represents the effective absorbance. SE_R, SE_A, and SE_M represent the reflection, absorption, and multiple internal reflection shielding effectiveness, respectively. While the SE_T is the total shielding effectiveness. Generally, SE_M can be negligible when SE_T exceeds 15 dB.

QUANTIFICATION AND STATISTICAL ANALYSIS

Origin software was used to compile and analyze data.